Oxidation Driven Thin-Film Solid-State Metal Dealloying Forming Bicontinuous Nanostructures

Cheng-Chu Chung, Charles Clark, Chonghang Zhao, Kim Kisslinger, Fernando Camino, Dmytro Nykypanchuk, Hui Zhong, Sanjit Ghose, Ruipeng Li, Chang-Yong Nam, and Yu-chen Karen Chen-Wiegart*

Solid-state metal dealloying (SSMD) is a promising method for fabricating nanoscale metallic composites and nanoporous metals across a range of materials. Thin-film SSMD is particularly attractive due to its ability to create fine features via solid-state interfacial reactions within a thin-film geometry, which can be integrated into devices for various applications. This work examines a new dealloying couple, namely the Nb–Al alloy with the dealloying agent Sc, as previously predicted in the machine-learning (ML) models. Prior ML predictions aimed to guide the design of nanoarchitectured materials through dealloying, relying on intuition-driven discovery within a large parameter space. However, this work reveals that at the nanoscale, the involvement of oxygen in thin film processing may instead drive the dealloying process, resulting in the formation of bicontinuous nanostructures similar to those formed by metal-agent dealloying. The phase evolution, as well as chemical and morphological changes, are closely analyzed using a combination of X-ray absorption spectroscopy, diffraction, and scanning transmission electron microscopy to understand the mechanisms behind nanostructure formation. The findings suggest a potential pathway for utilizing oxygen to drive the formation of bicontinuous metal–metal oxide nanocomposites, paving the way for further development of functional nanoporous materials in diverse fields.

1. Introduction

The dealloying process to create nanoarchitectured materials, including nanoporous materials and nanocomposites, has gained significant attention due to their various benefits, such as mechanical strength, lightweight, high surface-area-to-volume ratio, thermal, and electrical conductivities. These materials thus have found applications in nanotechnology for energy conversion,[1–6] mechanical engineering,[7–9] medicine,[10–12] and sensors,[13–18] Among different types of the dealloying processes in solid,[19–23] liquid,[7,24,25] and gas[26,27] media, the solid-state metal dealloying (SSMD) process, previously termed solid-state interfacial dealloying (SSID),[21–23] has emerged as a promising method for fabricating nanoarchitectured composites. In SSMD, a solid-state metallic solvent, referred to as the dealloying agent (element C), is used to induce a phase separation in a parent alloy (alloy AB) into A and B-C components. In prior studies of SSMD, the general principle for the material design considers mainly the thermodynamics,[28] primarily the mixing enthalpy and the enthalpy of formation. However, such a criterion deviates from the experimental observations. Moreover, the critical parameters and their interaction that determine the morphological, chemical, and structural evolution in SSMD remain unclear due to the large parameter space involved. The relationship between the resulting

C.-C. Chung, C. Clark, C. Zhao, C.-Y. Nam, Y.-c. K. Chen-Wiegart
Department of Materials Science and Chemical Engineering
Stony Brook University
Stony Brook, NY 11794, USA
E-mail: Karen.Chen-Wiegart@stonybrook.edu

K. Kisslinger, F. Camino, D. Nykypanchuk, C.-Y. Nam
Center for Functional Nanomaterials
Brookhaven National Laboratory
Upton, NY 11973, USA

H. Zhong
Department of Joint Photon Science Institute
Stony Brook University
Stony Brook, NY 11794, USA

S. Ghose, R. Li, Y.-c. K. Chen-Wiegart
National Synchrotron Light Source II
Brookhaven National Laboratory
Upton, NY 11973, USA

nanostructures and key processing parameters, such as parent alloy composition and crystallinity, dealloying time and temperature, as well as their corresponding atomic properties, is not yet fully understood. Furthermore, when applying the SSMD in a thin film geometry, additional factors such as thin-film thickness and interactions with the substrate need to be considered due to the geometric and dimensional conditions of thin films.

To gain a deeper understanding of the mechanisms involved in SSMD and thus enable to establish more comprehensive materials design principles, a framework incorporating machine-learning (ML)-augmented methods to explore the potential dealloying system has recently been demonstrated.[29] The goal of this prior work was to enable the creation of nanoarchitectured thin films through a closed-loop approach integrating ML-model prediction, combinatorial materials synthesis, and synchrotron X-ray autonomous characterization for experimental validation. Based on the outcomes of various ML models, potential dealloying systems were identified and proposed. While the framework for the experimental validation was proposed and tested using a previously developed dealloying system as a proof-of-concept, no investigation has been conducted on new dealloying systems predicted by the ML models. Therefore, the validity of the ML models and their predictions for new dealloying systems, as well as the inclusion of additional parameters in the models, remain uncertain.

In this work, we intend to validate one of the alloy combinations, Nb–Al/Sc, predicted by the ML method through a multimodal synchrotron analysis. In this system, Sc was chosen to be the solvent to selectively dealloy Al from the Nb. This system was chosen owing to two primary reasons: First, the Sc–Al pair has a lower mixing enthalpy compared to the Nb–Al and Nb–Sc pairs, which is consistent with the conventional design principle observed in other liquid and solid-state metal dealloying systems. This indicates Sc has the potential to drive the phase separation of the Nb–Al, resulting in the formation of a Nb/Sc–Al composite.[28] Although Sc has not been used as a dealloying solvent, exploring this new ternary dealloying system allows us to test a probable dealloying system that appears to be consistent with the conventional dealloying design principle. Second, the fabricated structure could be utilized as a Nb metal nanocomposite film or nanoporous Nb film after removing the residual Sc/Al containing phase(s). Nb possesses properties that are relevant to a wide range of applications, such as low neutron capture cross-section,[30] high thermal conductivity,[31] good corrosion resistance[31] and being physiologically inert,[32] and electrolytic capacitor.[33] Furthermore, an additional goal is to investigate the role of oxygen in SSMD. As it is often challenging to completely remove the oxygen from the sample processing, including the contribution from the substrates as well as during the thin-film deposition, heat treatment, and sample storage as well as transferring, how oxygen may influence the evolution of bicontinuous nanoarchitecture particularly in thin films when the surface-to-mass ratio is high, will be discussed. Future directions on how to further refine ML algorithms to predict and design dealloying systems will also be discussed. This proof-of-concept process demonstrates an oxygen-assisted dealloying process, highlighting the importance of considering metal oxidation as a parameter in the ML algorithm. Overall, this work emphasizes key directions for advancing the ML-augmented method,

enabling a more robust, rapid, and effective design of nanoarchitectured materials via solid-state metal dealloying.

2. Experimental Section

The thin-film SSMD methods had been previously developed and applied to various metallic systems, as mentioned in the introduction.[20–22] In this study, the method was applied and further developed specifically for the new system under investigation, as outlined below.

2.1. Thin-Film Synthesis with Sputtering and Heat-Treatment Process

The thin film deposition was conducted at the Center for Functional Nanomaterials (CFN) at Brookhaven National Laboratory (BNL). Two configurations of pristine alloy thin films were prepared: pure Nb–Al parent thin alloy film and Sc on top of Nb–Al bilayer thin film samples. The films were deposited with $\approx$(Nb–Al) 200 nm or (Sc) 200 nm/(Nb–Al) 200 nm thickness with an atomic ratio of 1:1 for Al:Sc. Silicon wafers were cut to 10×10 mm^2 and cleaned (sonicated in acetone and isopropyl alcohol for 10 min, respectively, and dried by compressed air), and used as the substrates (Rogue Valley Microdevices, USA). The thickness of the Si was 380 µm, with a layer of 2 µm SiO$_2$ on the surface, wet thermal oxide; the surface orientation of the Si wafers was (100). The deposition was conducted using a magnetron sputtering system (Kurt J. Lesker Company) at room temperature. The chamber was first evacuated to $\approx 3 \times 10^{-6}$ torr in pressure and then filled with Ar gas until the chamber pressure reached 4.7×10^{-3} torr. High-purity (99.95%, Nb/Al 40/60 at.% and 99.9% Sc) sputtering targets (Kurt J.Lesker Company) in a diameter of 3 inches (76.2 mm) were bombarded in sequence by Ar$^+$ ions from flowing pure Ar gas (99.9997%, Airgas, USA) at a pressure at 4×10^{-3} torr using direct-current (DC) power.

After the deposition process, an isothermal heat treatment was conducted on the thin-film samples in a tube furnace (Mini-Mite TF55030A) to introduce the dealloying process. The heat treatment processes were run in a reduced atmosphere (3% H$_2$ and 97% Ar) to reduce the tendency of oxidation. The samples were heated from room temperature to the target temperature using 30 °C min^{-1} as the ramping rate, held for a designated duration of time for different samples as detailed below, and cooled down to room temperature using cooling fans within 10 min. The various dealloying temperatures were selected to better understand the temperature-dependent dealloying behavior. The dealloying temperature was kept below the lowest melting point of the intermetallic compounds, specifically 1185 °C for the eutectic temperature of the Sc$_{78}$Al$_{22}$ alloy, to ensure the solid-state diffusion. Overall, the following conditions were used in this study, as listed in **Tables 1** and **2**.

2.2. Characterization of Surface and Cross-Sectional Morphology, Crystalline Phases, and Elemental Distribution

Materials characterization described below was also conducted at CFN of BNL.

Table 1. Thermal treatments for the thin-film Nb-Al-Sc system at a lower temperature with different temperatures and time duration for the analysis of chemical evolution. In the sample IDs, the solvent-metal-top configuration is noted as "smt", and the dealloying temperature in Celsius and time are denoted as "C" and "M" respectively.

Configuration	400 °C	500 °C	600 °C	650 °C		
		60 min		30 min	60 min	120 min
Sc on top of Nb-Al (solvent-metal-top)	smt-400C60M	smt-500C60M	smt-600C60M	smt-650C30M	smt-650C60M	smt-650C120M

2.2.1. Surface Analysis

JEOL 7600F scanning electron microscopy (SEM) with Oxford Instruments' energy dispersive spectroscopy (EDS) operating at 20 kV accelerating voltage was conducted to characterize the thin-film composition. Rigaku SmartLab X-ray Diffractometer (XRD) was used to obtain structural information of the thin film at room temperature. X-ray source with Cu-Kα radiation (λ = 1.54 Å) in grazing incidence diffraction (GID) mode with an angle of incidence of 5° was applied to generate the 1D X-ray diffraction pattern.

2.2.2. Cross-Sectional Analysis

Dual-beam scanning electron/focused ion beam microscope (FIB-SEM FEI Helios) was utilized to observe the cross-sectional morphology of the thin-film samples and prepare the lift-out specimens for transmission electron microscopy (TEM). A high-resolution analytical scanning/transmission electron microscope (S/TEM, FEI Talos F200X) operated at 200 kV was carried out to characterize the thin film in a nanoscale with high mass contrast. Equipped with the high-angle annular dark-field imaging (HAADF) and EDS, the STEM analysis was performed on the pristine and dealloyed samples for imaging the thin-film features and mapping the associated elemental distribution introduced by the dealloying process.

2.3. Synchrotron X-Ray Small-Angle Scattering

The morphology of the thin films was analyzed by grazing-incidence small-angle X-ray scattering at Complex Materials Scattering (CMS, 11-BM), at the National Synchrotron Light Source II (NSLS-II), BNL. The thin film samples were placed on the bar holders mounted in a vacuum chamber. The measurement was conducted using a 13.50 keV beam (where the wavelength was 0.9184 Å), with exposure time for 1 s. The scattering patterns were captured with a Dectris Pilatus 2M detector with a pixel size of 172 μm and 5 m sample-to-detector distance. The scattering

data was collected around the critical angle (0.1°–0.5°) to enhance the intensity of the targeted thin film. A 1D profile data was obtained by integrating a region of interest (0.004–1.0 Å^{-1}) from the scattering pattern for further quantitative analysis.

2.4. Synchrotron X-Ray Absorption Spectroscopy

Chemical information of the thin film was studied via X-ray absorption near-edge structure (XANES) spectroscopy at Beamline for Materials Measurement (BMM, 6-BM), at NSLS-II of BNL. The thin-film samples were placed on a horizontal wheel with a capacity to load up to eight samples; each of the sample holders was equipped with a spinning platform underneath to mitigate the issue of Bragg diffraction from the crystalline substrate, which will cause intensity change in the absorption spectra. The XANES spectra were collected from the thin-film samples on SiO$_2$/Si substrates in fluorescence mode. The measurement was conducted in a grazing-incidence geometry to provide a more surface-sensitive analysis to analyze the multi-layer thin films deposited on the substrates. Spectroscopic references including a Nb foil and Sc powders (99.9%, Sigma–Aldrich) were first measured in transmission mode before each scan on the sample for the energy calibration[34] and later used in the data processing. Two scans for Nb K-edge at 18 800–19 800 eV and six scans for Sc K-edge at 4300–5000 eV were collected and averaged[35] to further improve the signal-to-noise ratio of the absorption spectra.

2.5. Synchrotron X-Ray Diffraction

Phase evolution of the thin film materials was investigated via X-ray diffraction at X-ray Powder Diffraction (XPD, 28-ID-2), at NSLS-II of BNL. The thin film samples were mounted onto a frame holder with the surface of the thin film layer facing downstream to the detector to maximize the emitted signal from the sample surface. The diffraction patterns were collected from the thin film samples on SiO$_2$/Si substrate in transmission mode. A nickel (Ni) powder standard was first measured to calibrate the detector distance. The exposure time of the X-ray diffraction

Table 2. Thermal treatments for the thin-film Nb-Al-Sc system at a higher temperature with different temperatures and time duration for the analysis of structural and phase evolution. For the sample IDs, in addition to what is noted in Table 1, the parent-alloy configuration is noted as "pa".

Configuration	As-deposited	700 °C	900 °C			1100 °C
		60 min	0 min	7.5 min	60 min	60 min
Sc on top of Nb-Al (solvent-metal-top)	smt-pristine	smt-700C60M	–	–	smt-900C60M	smt-1100C60M
Pure Nb-Al (parent-alloy)	pa-pristine	–	pa-900C00M	pa-900C7p5M	pa-900C60M	–

ADVANCED
SCIENCE NEWS

www.advancedsciencenews.com

ADVANCED
MATERIALS
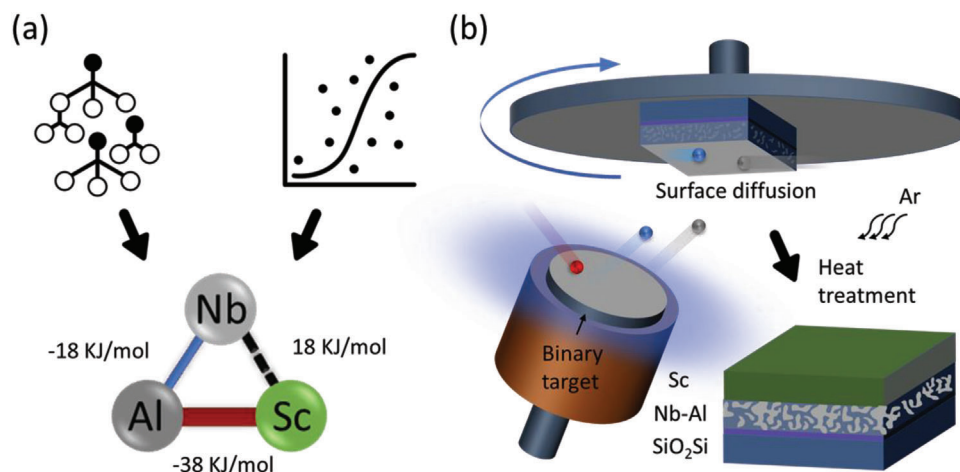INTERFACES

www.advmatinterfaces.de

Figure 1. Overview of the SSMD dealloying method and materials design: a) Dealloying system with the formation enthalpy predicted by machine-learning model. b) A schematic showing the DC sputtering process with binary alloy and thin-film evolution through SSMD process.

measurement on each sample was 20 min to ensure a sufficient signal-to-noise ratio of the diffraction patterns. The diffraction data were collected for a range of 0.01–10 Å^{-1} in reciprocal space.

3. Results and Discussion

3.1. Design and Composition of the Thin-Film Alloy

Through the ML models of dealloying using metals as a dealloying solvent (both in solid-state and liquid systems),[29] the Nb–Al–Sc system was first selected to validate the ML predictions. The predicted system in **Figure 1**a applied the Miedema's model,[36] having a formation enthalpy of −18 KJ mol^{-1} for the parent alloy Nb–Al, −38 KJ mol^{-1} for the Sc–Al dealloying elemental pair, and 18 KJ mol^{-1} for the immiscible elemental pair Nb–Sc. The thin-film system was prepared using the sputtering process, as depicted in Figure 1b, by sequentially depositing the binary alloy target Nb–Al and the metal target Sc onto SiO$_2$/Si. Two configurations of the deposited films on the SiO$_2$/Si substrates were the Nb–Al thin film with and without the Sc film on the top. More detailed information regarding the fabrication process is described in the Experimental Section. The purpose of these two configurations was first designed to study the influence of Sc on the dealloying process. With the dealloyed structure in the form of a nanoscaled film, it will also enable less ambiguous characterization with surface-sensitive techniques, such as synchrotron X-ray grazing-incidence small-angle X-ray scattering (GISAXS) and wide-angle X-ray scattering (GIWAXS).

The dealloying process was conducted through isothermal heat treatment using a tube furnace, with a flow of H$_2$ (3%, balanced with Ar) gas mixture, at various temperatures (400, 500, 600, 650, 700, 900, and 1100 °C) and different time duration (0, 7.5, 30, 60, and 120 min). Surface EDS analysis was used to confirm the elemental composition before and after the dealloying process. Figure S1 (Supporting Information) shows a comparison of the composition before and after the heating process. The as-deposited thin film consists of a 50–50 at.% ratio of Nb and Al. The composition of Nb and Al in the thin films treated at 900 and 1100 °C for 60 min remains consistent with the pristine thin

films (as-deposited and untreated), indicating the stability of the thin film under high temperatures.

3.2. Morphological Evolution with Thermal Treatment

The morphological evolution with thermal treatment is shown in **Figure 2**a–c through cross-sectional SEM images. The thin-film thickness remains ≈200 nm for each condition, indicating no material loss during the thermal treatment. The pristine thin film in both configurations (Figure S2, Supporting Information), parent-alloy and solvent-metal-top, shows a homogeneous morphology for the parent alloy (Nb–Al) and the dealloying metal (Sc) regions. With the treatment at 900 °C for 60 min, the morphology of the pristine thin film evolves into interconnected ligaments. These ligaments in the parent-alloy (pa) and solvent-metal-top (smt) present a fine feature size ≈15 nm. As the dealloying temperature is increased further to 1100 °C for the same time duration, the features in the Nb–Al region further increase, likely due to a coarsening process for minimizing surface energy as consistently observed in bicontinuous metal composites or porous structures prepared by dealloying.[37–44] Additionally, a temperature-dependent evolution of the feature morphology is observed, with the feature size growing from 15 to 30 nm as the temperature rises from 900 to 1100 °C.

These changes in size are also reflected in the position of the main scattering peak observed in the GISAXS analysis, as shown in Figure S2 (Supporting Information). The scattering vector (q) directly relates to the ligament–ligament spacing (d),[45–48] where $d \approx 2\pi/q$. The q values of ≈0.02 and ≈0.01 Å^{-1} correspond to d values of ≈31.4 nm and ≈62.8 nm for samples treated at 900 to 1100 °C, respectively. Since the two phases in the bicontinuous nanocomposite have similar feature sizes, the d value roughly corresponds to twice the ligament size. Therefore, based on the quantification of GISAXS, the estimated ligament size for the dealloyed Nb–Al treated at 900 to 1100 °C are ≈15.7 nm and ≈31.4 nm, respectively. In contrast, the morphology of the dealloying solvent layer shows no significant changes even at the higher heating temperature. This can be attributed to the limited
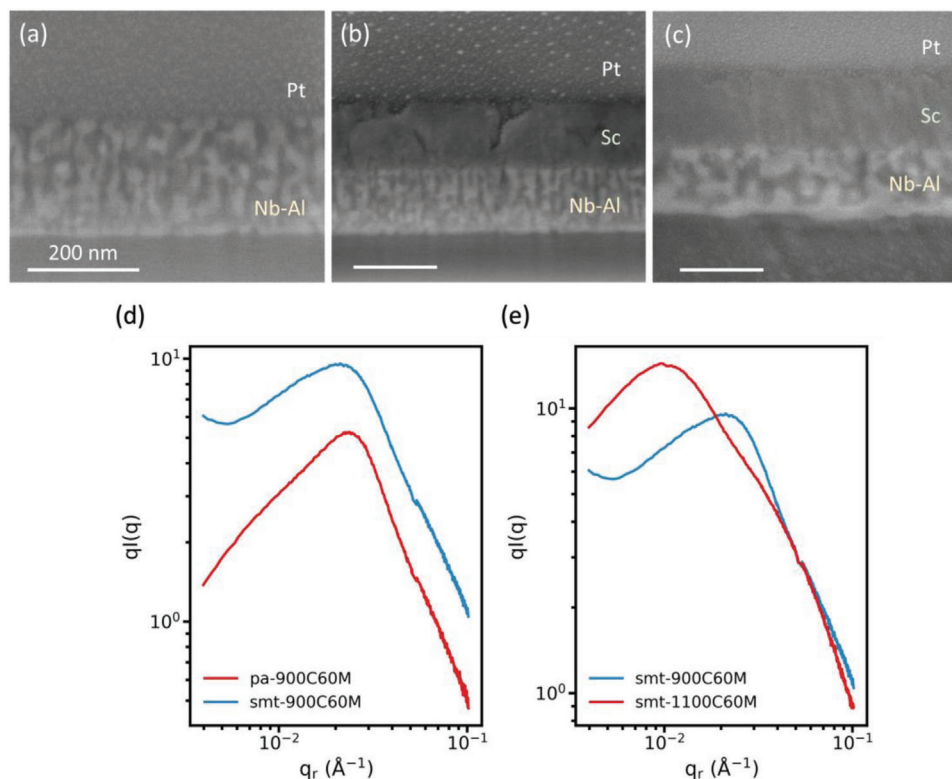
Figure 2. Morphological characterization of the dealloyed thin film. Cross-sectional images of parent-alloy (pa), and solvent-metal-top (smt) thin films after heating at 900 and 1100 °C for 60 min: a) pa-900C60M, b) smt-900C60M, and c) smt-1100C60M, respectively, on SiO₂/Si substrate with white scalebars in 200 nm. Comparison of GISAXS patterns of dealloyed thin film between different configurations d) pa-900C60M vs. smt-900C60M and different heating temperatures e) smt-900C60M vs. smt-1100C60M.

interaction between Sc and the parent alloy. In addition, the morphological evolution of the pure parent-alloy configuration indicates the bicontinuous structure can form in the absence of Sc (Figure S3, Supporting Information). Thus, it is likely that the morphological changes in the parent alloy may be induced by other elements.

3.3. Phase Separation and Elemental Distribution of the Dealloying Features

Figure 3 presents the STEM EDX analysis of the as-sputtered parent alloy, which reveals the elemental distribution within the precursor alloy and indicates chemical homogeneity. Under thermal treatment at 900 °C for 60 min, the Nb evolves into interconnected ligaments, indicating a bicontinuous nanostructure was formed in the system. With the addition of the solvent metal Sc on top of the parent alloy, the resulting continuous feature closely resembles that of the pure parent-alloy configuration. In Figure 3d, the two elements, Nb- and Al-rich phases, are separated after the thermal treatment at 900 °C for 60 min. However, the evolution of ligaments in the Nb–Al dealloying region occurs independently, without interdiffusion with the Sc layer or the SiO₂/Si substrates. Conversely, there is no significantly morphological evolution in the Sc film from the heat treatment, suggesting the element does not react with the parent alloy Nb–Al

thin film. While this finding is not consistent with the initial prediction – using Sc to drive the dealloying of Nb–Al alloy – the resulting morphology is still a bicontinuous nanostructure. This indicates that a different component may be driving the dealloying process, possibly through a distinct mechanism. To better understand the mechanism, it is therefore interesting to understand the effects of unknown factors within the predicted ternary system with the specific configuration.

3.4. Chemical Evolution with Different Temperatures and Time Duration

To gain a deeper understanding of the elemental reaction in the system, a study was conducted to investigate the chemical evolution of the solvent-metal-top configuration under various treatment temperatures and time durations. From the X-ray absorption spectroscopy shown in **Figure 4**, the XANES spectroscopic analysis reveals the changes in the chemical composition and oxidation state of the dealloyed thin film. At the lower temperatures, from 400 to 700 °C, a feature just above the Nb K-edge (indicated by a black dashed arrow) in the XANES spectra demonstrates a slight evolution toward the feature corresponding to the pure Nb. This evolution is indicative of a chemical change occurring in the system, suggesting the presence of a purer Nb phase at a higher heating temperature. As for the treatment concerning the
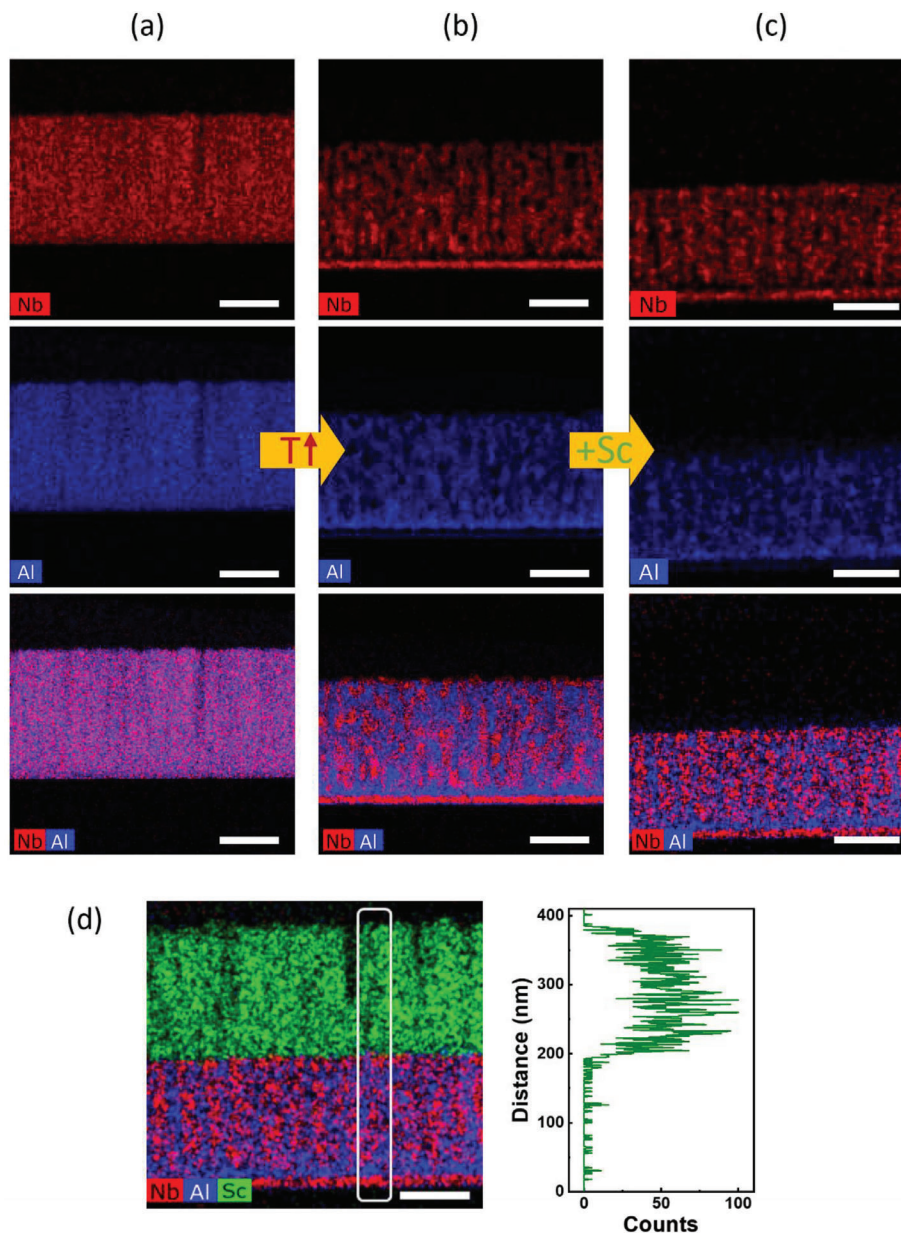
**ADVANCED
SCIENCE NEWS**

www.advancedsciencenews.com

**ADVANCED
MATERIALS
INTERFACES**

www.advmatinterfaces.de

Figure 3. STEM characterization with HAADF EDX of the Nb, Al, and Nb-Al distributions on parent-alloy (pa) a) pa-pristine, b) pa-900C60M, and solvent-metal-top (smt) c) smt-900C60M thin film, and d) configuration of the system with Nb, Al, Sc elements characterization (The white square is the region of interest for the Sc content presented in the line-scan profiles.) on SiO_2/Si substrate with white scale bars in 100 nm.

time-dependent condition, the thin film subjected to a 30 min heating process reveals relatively stable changes in the chemical state of the Nb-containing phases. No further chemical evolution was observed in the sample treated for 120 min, compared to the one treated for 60 min.

On the other hand, the Sc K-edge absorption presents no significant shift, but there are sharper pre-edge and prominent peaks over time and temperatures, changing toward the feature of Sc_2O_3 K-edge energy. A comparison between the Sc XANES spectrum from the pristine sample and the XANES spectra of metallic Sc and Sc oxides reveals that the solvent metal (Sc) had already been slightly oxidized before the isothermal treatment.

Furthermore, the Sc phase remains stable as oxides during the heat treatment rather than dissolving the target element (Al) from the parent alloy (Nb–Al).

3.5. Structural and Phase Evolution Under High Temperature

Figure 5a–c shows the XANES analysis of samples treated above 900 °C, providing insight into the dealloying process discussed in Section 3.2. Under the higher temperature above 900 °C, the Nb XANES spectra of the samples prepared with the parent-alloy and solvent-metal-top configurations resemble that of pure Nb
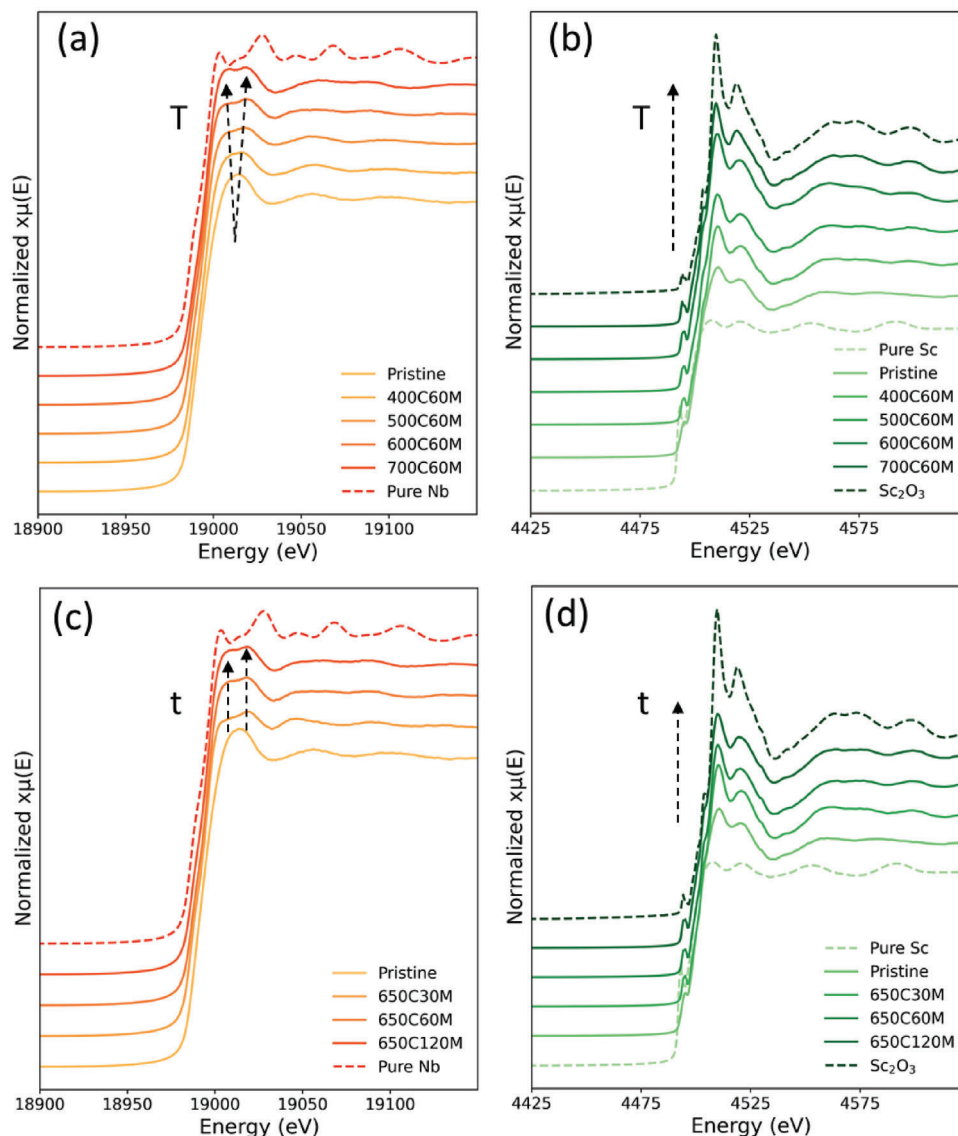
**ADVANCED
SCIENCE NEWS**

www.advancedsciencenews.com

**ADVANCED
MATERIALS
INTERFACES**
Open Access

www.advmatinterfaces.de

Figure 4. Chemical evolution of solvent-metal-top (smt) thin film in a,c) Nb and b,d) Sc K-edge absorption energy with temperature-dependent (400, 500, 600, and 700 °C) relation for 60 min and time-dependent (30, 60, and 120 min) relation at 650 °C.

along the black arrow in Figure 5a,b. However, the above-edge Nb XANES feature at 1100 °C shows an opposite shift toward the lower energy in the solvent-metal-top films, as indicated by a red arrow in Figure 5c. This shift signifies a change in the chemical state away from pure Nb, suggesting the formation of a new compound as evidenced by the evolution of the peak feature.

The crystalline structures of the Nb- and Al-rich phases in both configurations after thermal treatment were further analyzed by XRD to understand the structural evolution, as shown in Figure 5d–f. The as-deposited thin film displays a broad background without sharp peaks, indicating that the pristine films are amorphous. These findings support the existence of mixing phases in the initial state and the absence of phase separation. At 700 °C, the presence of the Nb, Al_2O_3, and Sc_2O_3 main peaks indicates the initiation of structural evolution. At 900 °C, the Al_2O_3

phase is observed in all configurations, but addition of Nb_3Si and Nb_5Si_3 phases shows in the XRD patterns of the parent-alloy and solvent-metal-top samples, respectively. The Nb_5Si_3 phase remains stable in the thin films subjected to thermal treatment at 1100 °C. The elemental distribution of silicon in Figure S4 (Supporting Information) shows that Si may not be the critical factor driving the structural evolution. The Si does not diffuse into the bi-continuous region of the solvent-metal-top configuration at 900 °C, or only partially diffuses into that region at 1100 °C. No intermetallic compounds of Nb_xAl_y or Sc_xAl_y phases are observed, suggesting that the two phases in the bicontinuous structure shown in HAADF EDX are pure niobium (Nb) and aluminum oxide (Al_2O_3). These two phases present distinct phase separation, indicating that scandium (Sc), although originally intends as a dealloying solvent, does not dissolve the target element, aluminum (Al), in this system.
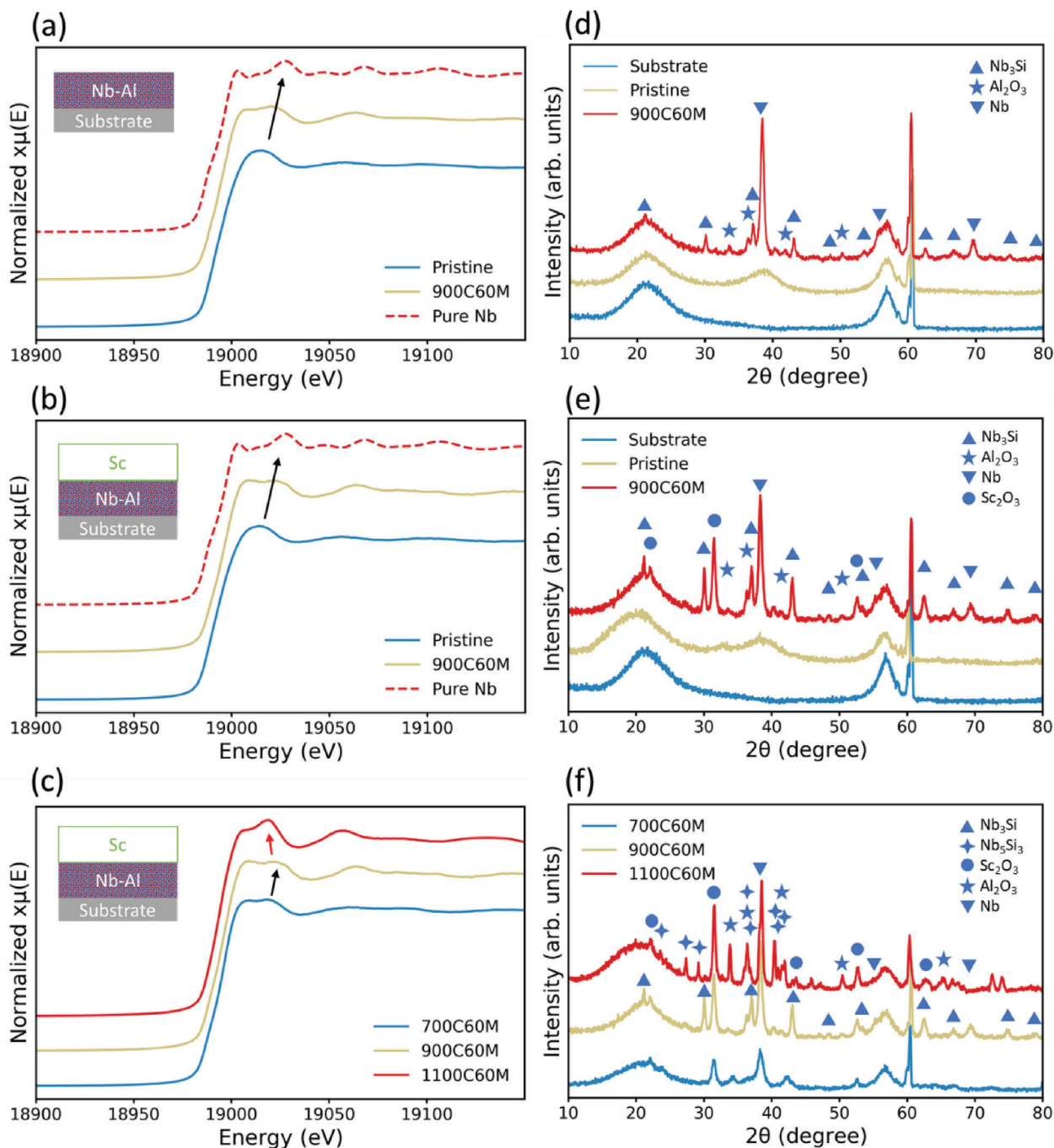
**ADVANCED
SCIENCE NEWS**

www.advancedsciencenews.com

**ADVANCED
MATERIALS
INTERFACES**
Open Access

www.advmatinterfaces.de

Figure 5. Chemical evolution of a) parent-alloy (pa) and b,c) solvent-metal-top (smt) thin films shown in Nb K-edge XANES spectra, dealloyed at higher temperatures (700, 900, and 1100 °C) for 60 min. d–f) Structural evolution of the corresponding configurations with phase identification by X-ray diffraction. Normalized xμ (E) is the normalized, energy (E) dependent X-ray absorption signal.

3.6. Formation of Bicontinuous Nanoarchitecture

Here, the mechanisms behind the formation of the bicontinuous structure in the Nb–Al system in the absence of another metallic solvent will be discussed based on the characterizations presented in the prior sections. In the sample with the solvent-metal-top configuration at 900 °C, the parent alloy containing

Nb reacts directly with SiO_2, forming a metal-rich silicide phase, Nb_3Si, at the interface between the parent alloy and the substrate (Figure S4, Supporting Information).[49,50] Oxygen, dissociated from the SiO_2, diffuses into the parent alloy layer, as illustrated in **Figure 6**. Although pure Nb is observed in the reacted thin film based on the diffraction results (Figure S5, Supporting Information), the oxygen is distributed throughout the
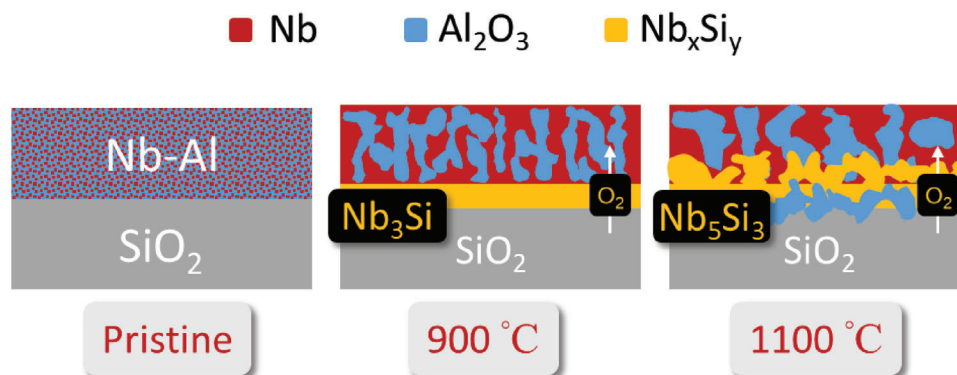
2300454 (8 of 11)

**ADVANCED
SCIENCE NEWS**

www.advancedsciencenews.com

**ADVANCED
MATERIALS
INTERFACES**

www.advmatinterfaces.de

Figure 6. A schematic illustrating the oxygen source from the SiO$_2$/Si substrate. Oxygen diffusion path in parent-alloy (pa) configuration from the reaction between metal and silicon oxide.

parent-alloy layer, overlapping with Nb and Al (Figure S6, Supporting Information), indicating the coexistence of pure metal and metal oxides. Given the amount of oxygen present in the thin film, there is a possibility that oxygen from the surrounding environment may also be involved. Notably, due to the oxygen leaving in the layer of the parent alloy, Al can form oxides into Al$_2$O$_3$. The presence of the metal oxides at the interface of Nb/Al restricts the reorganization of the metal atoms by slowing down their interface/surface diffusion. This constraint could lead to the formation of a bicontinuous structure with finer dealloyed features when the Nb/Al$_2$O$_3$ phase separation occurs in conjunction with Al oxidation compared to the absence of the oxidation process. As the temperature increases to 1100 °C, the Nb$_5$Si$_3$ phase remains stable. Meanwhile, the oxygen preferably reacts with Al rather than Nb, forming internal oxide in the parent alloy at high temperatures, leaving the Nb atoms behind.[51] The Nb phase, therefore, further coarsens into larger ligaments.

Here an alternative mechanism is also considered to explain the formation of bicontinuous nanostructures, such as using phase separation in precursor alloys as a method to fabricate bicontinuous nanoporous materials. The method has been reported in the literature, including metallic glasses Zr$_{47}$Cu$_{46}$Al$_7$-Y$_{47}$Cu$_{46}$Al$_7$[52] and co-sputtered Cu–Mo thin film.[53,54] Although the phase separation followed by the coarsening may seem to be a plausible mechanism,[55,56] our Nb–Al binary system did not separate into intermetallic phases, such as NbAl$_3$, Nb$_2$Al, and Nb$_3$Al.[57] Besides, compared to the phase separation due to a large miscible gap in the systems listed above, the Nb–Al pair is a miscible binary with negative heat of mixing enthalpy (−18 kJ mol^{-1}), indicating a tendency to form intermetallic compounds when the system reaches stability. In other words, the Nb–Al would not transform into pure Nb and pure Al phases via a spontaneous reaction. Instead, the formation of the Nb and Al oxides suggests that not only a side reaction occurs after the phase separation, but oxidation plays a role in affecting the kinetics of the phase separation.

4. Conclusion

The design of nanocomposite with bi-continuous nanoarchitecture using SSMD process through the ML method has been

examined and discussed. Based on the result of the ML training the data from the literature, the Nb–Al/Sc system following Miedema's model was first selected toward validating the ML algorithm. Two configurations, solvent-metal-top and parent-alloy only thin films, were deposited to further study the differences between them during the dealloying process. SiO$_2$/Si substrate was applied to provide an apt platform for developing various dealloying systems. SEM-FIB and HAADF EDX techniques were conducted to characterize the morphological and elemental evolution of the dealloyed thin films. The dealloyed features evolve from an amorphous thin film to a film containing ligaments-like nanostructures ranging from 15 to 30 nm after the heating process. EDX mapping visualizes the elemental distribution of nanostructures, with feature sizes consistent with the GISAXS analysis.

Chemical and structural evolution were identified by XANES and XRD techniques. At the elevated temperature, the amorphous Nb transforms into a crystalline structure, and an additional Al$_2$O$_3$ starts to form. Scandium, predicted as a dealloying agent, does not participate in the dealloying process. In the case of the pure parent-alloy configuration at 900 °C, the phase separation shows the evidence of self-organization without Sc, indicating a third element, oxygen, plays a role in the evolution of bi-continuous nanostructure. The oxygen was found to drive the formation of the bicontinuous metal–metal oxide nanostructure through the oxidation of the more reactive metal (Al) in the parent alloy (Nb–Al), forming a bicontinuous structure consisting of Al$_2$O$_3$ and metallic Nb. Simultaneously, silicon from the substrate forming a silicide phase with metal may have a minor effect on the feature evolution. Future work can explore the use of different types of substrates, such as sapphire, diamond, or TaN, to minimize interdiffusion with the substrate. Furthermore, as a result of the validation process, the ML algorithm will need to be further improved, considering factors including oxidation, intermetallic compound formation, alloy composition, and kinetic parameters. By developing the ML-augmented model further, more accurate predictions of potential dealloying systems can be achieved, ultimately realizing the concept of 'materials by design' for nanoarchitectured materials. The oxidation-driven process proposed in this work can also be intentionally applied in solid-state dealloying to create bicontinuous nanocomposites for future applications.

Conflict of Interest

The authors declare no conflict of interest.

Author Contributions

C.-C.C. and Y.-c.K.C.-W. proposed the research idea with the input from C.Z., Y.-c.K.C.-W., and C.Z. wrote the user proposals for the BMM beamlines at NSLS-II, BNL, and instruments at CFN. C.-C.C. and C.C. conducted the DC sputtering deposition of NbAl and Sc at CFN, BNL, and heating process at Stony Brook University. H.Z. and S.G. set up and supervised C.-C.C. and C.C. during the synchrotron X-ray diffraction experiment, guiding the data analysis. R.L. set up and supervised C.-C.C. for the synchrotron small-angle X-ray scattering experiment, providing support on the data analysis. C.-C.C. and C.C. conducted the synchrotron X-ray absorption experiments under the guidance of Y.-c.K.C.-W.; C.-C.C. was trained by C.-C.N. and operated the sputtering deposition; C.-C.C. was trained and conducted the XRD diffraction analysis under the guidance of D.N. at CFN; F.C. trained C.-C.C. to characterize the cross-sectional images using the FIB-SEM at CFN. For the TEM sample preparation and STEM analysis at CFN, K.K. provided training to C.-C.C.; C.-C.C. conducted the TEM sample preparation with FIB-SEM lift-out as well as the STEM imaging and EDS analysis under the supervision and guidance of K.K.; C.-C.C. and Y.-c.K.C.-W. wrote the manuscript, with inputs from all coauthors.

Data Availability Statement

The data that support the findings of this study are available from the corresponding author upon reasonable request.

[1] Y. Ding, M. W. Chen, J. Erlebacher, *J. Am. Chem. Soc.* **2004**, *126*, 6876.

[2] V. Zielasek, B. Jurgens, C. Schulz, J. Biener, M. M. Biener, A. V. Hamza, M. Baumer, *Angew Chem., Int. Ed.* **2006**, *45*, 8241.

[3] R. Y. Wang, C. X. Xu, X. X. Bi, Y. Ding, *Environ. Sci.* **2012**, *5*, 5281.

[4] R. Song, J. Han, M. Okugawa, R. Belosludov, T. Wada, J. Jiang, D. Wei, A. Kudo, Y. Tian, M. Chen, H. Kato, *Nat. Commun.* **2022**, *13*, 5157.

[5] Q. Sang, S. Hao, J. Han, Y. Ding, *EnergyChem* **2022**, *4*, 100069.

[6] Y. Li, Q. Zhang, X. Zhao, H. Wu, X. Wang, Y. Zeng, Q. Chen, M. Chen, P. Liu, *Adv. Funct. Mater.* **2023**, *33*, 2214124.

[7] I. McCue, S. Ryan, K. Hemker, X. D. Xu, N. Li, M. W. Chen, J. Erlebacher, *Adv. Eng. Mater.* **2016**, *18*, 46.

[8] I. V. Okulov, A. V. Okulov, A. S. Volegov, J. Markmann, *Scr. Mater.* **2018**, *154*, 68.

[9] I. V. Okulov, A. V. Okulov, I. V. Soldatov, B. Luthringer, R. Willumeit-Romer, T. Wada, H. Kato, J. Weissmuller, J. Markmann, *Mat. Sci. Eng. C-Mater.* **2018**, *88*, 95.

[10] M. Heiden, S. Huang, E. Nauman, D. Johnson, L. Stanciu, *J. Biomed. Mater. Res. A* **2016**, *104*, 1747.

[11] I. V. Okulov, J. Weissmüller, J. Markmann, *Stem Cells Int.* **2017**, *7*, 20.

[12] A. V. Okulov, A. S. Volegov, J. Weissmuller, J. Markmann, I. V. Okulov, *Scr. Mater.* **2018**, *146*, 290.

[13] Z. Liu, P. C. Searson, *J. Phys. Chem. B* **2006**, *110*, 4318.

[14] L. H. Qian, X. Q. Yan, T. Fujita, A. Inoue, M. W. Chen, *Appl. Phys. Lett.* **2007**, *90*, 153120.

[15] L. Y. Chen, X. Y. Lang, T. Fujita, M. W. Chen, *Scr. Mater.* **2011**, *65*, 17.

[16] D. Y. Zhao, G. L. Yu, K. L. Tian, C. X. Xu, *Biosens. Bioelectron.* **2016**, *82*, 119.

[17] H. Yang, J. Zhao, M. J. Qiu, P. Sun, D. X. Han, L. Niu, G. F. Cui, *Biosens. Bioelectron.* **2019**, *124*, 191.

[18] Z. Yang, Z. Lin, J. Yang, J. Wang, J. Yue, B. Liu, L. Jiang, *Appl. Surf. Sci.* **2022**, *579*, 152130.

[19] T. Wada, K. Yubuta, H. Kato, *Scr Mater.* **2016**, *118*, 33.

[20] I. McCue, M. J. Demkowicz, *JOM* **2017**, *69*, 2199.

[21] C. Zhao, K. Kisslinger, X. Huang, M. Lu, F. Camino, C.-H. Lin, H. Yan, E. Nazaretski, Y. Chu, B. Ravel, M. Liu, Y.-c. K. Chen-Wiegart, *Mater Horiz.* **2019**, *6*, 1991.

[22] C. Zhao, K. Kisslinger, X. Huang, J. Bai, X. Liu, C.-H. Lin, L.-C. Yu, M. Lu, X. Tong, H. Zhong, A. Pattammattel, H. Yan, Y. Chu, S. Ghose, M. Liu, Y.-c. K. Chen-Wiegart, *Nanoscale* **2021**, *13*, 177256.

[23] C. Zhao, L.-C. Yu, K. Kisslinger, C. Clark, C.-C. Chung, R. Li, M. Fukuto, M. Lu, J. Bai, X. Liu, H. Zhong, M. Liu, S. Ghose, Y.-c. K. Chen-Wiegart, *Acta Mater.* **2023**, *242*, 118433.

[24] J. Erlebacher, M. J. Aziz, A. Karma, N. Dimitrov, K. Sieradzki, *Nature* **2001**, *410*, 450.

[25] L. Sun, C. L. Chien, P. C. Searson, *Chem. Mater.* **2004**, *16*, 3125.

[26] Z. Lu, C. Li, J. Han, F. Zhang, P. Liu, H. Wang, Z. Wang, C. Cheng, L. Chen, A. Hirata, T. Fujita, J. Erlebacher, M. Chen, *Nat. Commun.* **2018**, *9*, 276.

[27] Z. Lu, F. Zhang, D. Wei, J. Han, Y. Xia, J. Jiang, M. Zhong, A. Hirata, K. Watanabe, A. Karma, J. Erlebacher, M. Chen, *Acta Mater.* **2021**, *212*, 116916.

[28] A. R. Miedema, P. F. Dechatel, F. R. Deboer, *Phys. B* **1980**, *100*, 1.

[29] C. Zhao, C.-C. Chung, S. Jiang, M. M. Noack, J.-H. Chen, K. Manandhar, J. Lynch, H. Zhong, W. Zhu, P. Maffettone, D. Olds, M. Fukuto, I. Takeuchi, S. Ghose, T. Caswell, K. G. Yager, Y.-c. K. Chen-Wiegart, *Commun. Mater.* **2022**, *3*, 86.

[30] B. Lawriniang, R. Ghosh, S. Badwar, V. Vansola, Y. S. Sheela, S. V. Suryanarayana, H. Naik, Y. P. Naik, B. Jyrwa, *Nucl. Phys. A* **2018**, *973*, 79.

[31] D. C. Goldberg, G. Dicker, S. A. Worcester, *Nucl. Eng. Des.* **1972**, *22*, 124.

**ADVANCED
SCIENCE NEWS**

www.advancedsciencenews.com

**ADVANCED
MATERIALS
INTERFACES**
Open Access

www.advmatinterfaces.de

[32] R. Godley, D. Starosvetsky, I. Gotman, *J. Mater. Sci-Mater. M* **2004**, *15*, 1073.

[33] J. W. Kim, M. Tsuda, T. Wada, K. Yubuta, S. G. Kim, H. Kato, *Acta Mater.* **2015**, *84*, 497.

[34] B. Ravel, M. Newville, *J. Synchrotron Radiat.* **2005**, *12*, 537.

[35] M. Newville, *J. Phys.: Conf. Ser.* **2013**, *430*, 012007.

[36] A. Takeuchi, A. Inoue, *Mater. Trans.* **2005**, *46*, 2817.

[37] L. H. Qian, M. W. Chen, *Appl. Phys. Lett.* **2007**, *91*, 083105.

[38] M. Hakamada, M. Mabuchi, *J. Mater. Res.* **2009**, *24*, 301.

[39] M. E. Cox, D. C. Dunand, *Mat. Sci. Eng. A* **2011**, *528*, 2401.

[40] J. Erlebacher, *Phys. Rev. Lett.* **2011**, *106*, 225504.

[41] Y.-c. Chen-Wiegart, S. Wang, Y. S. Chu, W. L. Liu, I. McNulty, P. W. Voorhees, D. C. Dunand, *Acta Mater.* **2012**, *60*, 4972.

[42] M. Tsuda, T. Wada, H. Kato, *J. Appl. Phys.* **2013**, *114*, 113503.

[43] Y. Li, B.-N. Dinh Ngô, J. Markmann, J. Weissmüller, *Phys. Rev. Mater.* **2019**, *3*, 076001.

[44] K. L. M. Elder, W. B. Andrews, M. Ziehmer, N. Mameka, C. Kirchlechner, A. Davydok, J.-S. Micha, A. F. Chadwick, E. T. Lilleodden, K. Thornton, P. W. Voorhees, *Proc. Natl. Acad. Sci. USA* **2021**, *118*, e2104132118.

[45] S. S. Welborn, E. Detsi, *Nanoscale Horiz.* **2020**, *5*, 12.

[46] S. S. Welborn, S. van der Meer, J. S. Corsi, J. T. M. de Hosson, E. Detsi, *ACS Appl. Mater. Interfaces* **2021**, *13*, 117211.

[47] A. K. Ng, S. S. Welborn, E. Detsi, *Scr. Mater.* **2022**, *206*, 114215.

[48] M. Gossler, E. Hengge, M. Bogar, M. Albu, D. Knez, H. Amenitsch, R. Wurschum, *J. Phys. Chem. C* **2022**, *126*, 4037.

[49] S. Q. Wang, J. W. Mayer, *J. Appl. Phys.* **1990**, *67*, 2932.

[50] O. M. Ndwandwe, Q. Y. Hlatshwayo, R. Pretorius, *Mater. Chem. Phys.* **2005**, *92*, 487.

[51] S. Hayashi, S. Takagi, R. Yamagata, T. Narita, S. Ukai, *Oxid. Met.* **2012**, *78*, 167.

[52] W. Jiao, P. Liu, H. Lin, W. Zhou, Z. Wang, T. Fujita, A. Hirata, H.-W. Li, M. Chen, *Chem. Mater.* **2017**, *29*, 4478.

[53] B. Derby, Y. Cui, J. K. Baldwin, A. Misra, *Thin Solid Films* **2018**, *647*, 50.

[54] Y. Lu, B. Derby, H. Sriram, K. Kadirvel, C. P. Wang, X. J. Liu, A. Misra, Y. Z. Wang, *Acta Mater.* **2021**, *220*, 117313.

[55] J. Yu, X. Zhou, C. Zhang, *Mater. Lett.* **2012**, *69*, 13.

[56] Y. Tan, H. Wang, P. Liu, C. Cheng, F. Zhu, A. Hirata, M. Chen, *Adv. Mater.* **2016**, *28*, 2951.

[57] H. Sina, S. Iyengar, *J. Alloys Compd.* **2015**, *628*, 9.